4D-printed shape memory polymer

Modeling and fabrication

Noroozi, Reza; Zolfagharian, Ali; Fotouhi, Mohammad; Bodaghi, Mahdi

DOI
10.1016/B978-0-323-95430-3.00007-5

Publication date
2022

Document Version
Final published version

Published in
Smart Materials in Additive Manufacturing, volume 2

4D-printed shape memory polymer: Modeling and fabrication

7

Reza Noroozi[a,b], *Ali Zolfagharian*[c], *Mohammad Fotouhi*[d], *and Mahdi Bodaghi*[a]
[a]Department of Engineering, School of Science and Technology, Nottingham Trent University, Nottingham, United Kingdom
[b]Faculty of Engineering, School of Mechanical Engineering, University of Tehran, Tehran, Iran
[c]School of Engineering, Deakin University, Geelong, VIC, Australia
[d]Department of Materials, Mechanics, Management & Design (3MD), Delft University of Technology, Delft, Netherlands

Introduction

Additive manufacturing (AM), also known as three-dimensional (3D) printing, as one of the most potent manufacturing methods, is fabricating a 3D structure using computer-aided design (CAD) data or computed tomography (CT) scan under computer control by adding material layer by layer (Askari et al., 2021; Attaran, 2017; Shirzad, Zolfagharian, Matbouei, & Bodaghi, 2021; Soltani, Noroozi, Bodaghi, Zolfagharian, & Hedayati, 2020; Wong & Hernandez, 2012; Yan et al., 2018; Zolfagharian, Kaynak, et al., 2020; Zolfagharian, Denk, et al., 2020). In contrast to traditional manufacturing processes that start from raw block material and remove waste materials, the AM process can demonstrate better aspects, such as freedom of design, reduced postprocessing, waste reduction, faster construction, and lower cost, and provide the opportunity for the fabrication of a complex structure (Levy et al., 2018; Ngo, Kashani, Imbalzano, Nguyen, & Hui, 2018; Soltani et al., 2020; Sun, Ma, Huang, Zhang, & Qian, 2020; Zadpoor & Malda, 2017). Researchers have been developed various methods for 3D printing, such as fused deposition modeling (FDM), selective laser melting (SLM), and stereolithography (SLA), due to the importance and application of 3D printing technology in different industries (Dudek, 2013; Ngo et al., 2018; Shahrubudin, Lee, & Ramlan, 2019). The SLM is one of the AM-metal-base processes in which a 3D part is created by applying laser energy to powder beds. In this method, by using a laser in the powder area, each layer is melted to the required cross section, and then, the melted powder particles bond and solidify. This process continues until the 3D object is created (Olakanmi, Cochrane, & Dalgarno, 2015). The FDM process is one of the most popular methods among printing methods due to its simplicity, accessibility, low cost, and ability to use different materials (Rayegani & Onwubolu, 2014). In this method, in order to create a specific object, a moving nozzle fused a thermoplastic continuous filament on a bed (Penumakala, Santo, & Thomas, 2020; Rayegani & Onwubolu, 2014). Although 3D printing technology has evolved over time, there are still some limitations and challenges, such as scalability, directional dependency, and structure rigidity, which could not change

Smart Materials in Additive Manufacturing, Volume 2: 4D Printing Mechanics, Modeling, and Advanced Engineering Applications
https://doi.org/10.1016/B978-0-323-95430-3.00007-5

their shape and property over time (Ahmed et al., 2020; El-Sayegh, Romdhane, & Manjikian, 2020). For example, recent researchers have found that 3D-printed sample characterizations are dependent on various input parameters, such as printing speed, orientation, print temperature, which make the predictability of the sample features challenging.

With the advent of 3D printing technology, the concept of 4D printing technology was introduced by Tibbits in 2013, and some of the challenges and limitations of 3D printing technology were overcome (Tibbits, 2014). 4D printing technology has added a fourth dimension to 3D printing technology, which displays the time. In other words, the fourth dimension is that printed structures are a function of time (Askari et al., 2021; Attaran, 2017; Bodaghi et al., 2020; Bodaghi & Liao, 2019; Damanpack, Bodaghi, & Liao, 2020; Shirzad et al., 2021; Soltani et al., 2020; Wong & Hernandez, 2012; Yan et al., 2018; Zolfagharian, Denk, et al., 2020; Zolfagharian et al., 2021). In 4D-printed structures, in contrast to 3D printing technology, which constructs 3D-static objects, dynamic structures with the ability to change shape and color are built. Static structures, which are printed with active materials, under external stimuli such as thermal, humidity, light, and electric or magnetic field, exhibit a dynamic behavior such as self-sensing, self-actuating, and shape-changing (Khoo et al., 2015; Shie et al., 2019; Zhang, Demir, & Gu, 2019). Active materials, such as shape memory polymers, should be used in the printing process in order to print structures with dynamic properties. Shape memory polymers (SMPs) have received more attention due to their lower cost, lower density, high recoverable strain, simple shape programming process, and excellent controllability over the recovery process (Bodaghi, Noroozi, Zolfagharian, Fotouhi, & Norouzi, 2019; Jebellat, Baniassadi, Moshki, Wang, & Baghani, 2020; Leng, Lu, Liu, Huang, & Du, 2009). Significant research has been conducted on 4D printing technology due to its vast potential. For example, in a study, the commercial polymer, SU-8, was employed in 4D printing self-morphing structures in which the shape transformation is driven via a swellable guest medium (Su et al., 2018). Using the self-folding mechanism by other researchers, a biomedical application that can be used as a cardiac stent was introduced. To model the thermomechanical behavior of structures, they used the phase transformation approach, drove equilibrium equations, and solved them using an in-house code (Bodaghi, Damanpack, & Liao, 2017). Since the printing parameters have a significant effect on sample performance, the effect of filament size, orientation, air pump pressure, and the filling pattern was studied on the shape transformation. To model the shape transformation mechanism, a hyperelastic model was employed for the SU-8 polymer (Su et al., 2018). Another research investigated programming SMP during the FDM process. In this regard, the dynamic structures shape their configuration from 1D to 2D and 1D to 2D-3D under the thermal stimulus. After shape transformation, self-folding structures made of SMP could not be folded or unfolded at temperatures lower than glass transition. To settle this issue, in a study, by using the FDM process, a novel self-folding mechanism was designed. They fabricated a hybrid hinge that was made of a soft elastomer and a 4D printing element. They also validated their experimental result with COMSOL-based finite element simulation (Yamamura & Iwase, 2021).

The literature review reveals that the fabrication and modeling of 4D printing components are extremely important and many researchers have done various studies on 4D printing and its applications. Therefore, in this chapter, first, the concept of the shape memory effect is described, and then, based on the SMPs cycle, the 4D printing programming during the FDM process is explained. Due to the complexity and difficulties of employing shape memory constitutive equations in finite element software to model 4D-printed elements, a simple method based on the 4D printing concept is proposed. The proposed model has been calibrated based on experiments and, as case studies, some of the smart structures are designed and modeled in finite element software.

4D printing programming

In this section, by considering the shape memory effect (SME) and FDM process, the concept of 4D printing, for 3D-printed samples during manufacturing, is described. The temperature-sensitive SMPs are a class of active material in which temperature plays a triggering role. As shown in Fig. 7.1, shape memory cycling consists of four stages. At the first step, the sample is heated up to the T_h, which is higher than the glassy transition temperature (T_g). At the constant temperature (T_h), the sample is loaded and transformed to the desired shape, and then, the sample is cooled down until T_g, which is lower than glassy transition temperature. In the next step, the mechanical constraints are removed and an inelastic strain, called prestrain, remains in the sample, which causes programmed shape (after a small elastic deformation). The programmed shape is a free-state configuration that is stable in lower temperatures than T_g. When it is needed, the sample could be reheated and recovered to its original (permanent) shape; this step is called the shape recovery process.

In the FDM technology, a thermomechanical cycle similar to shape memory programming is applied to the sample during the printing process. So, it may have the potential to print a 4D SMP architecture with shape programming simultaneously. Fig. 7.2 shows a schematic of 3D printing technology. The FDM technology is based on melting raw materials. Therefore, in the first step, the filament heated up until T_{in}

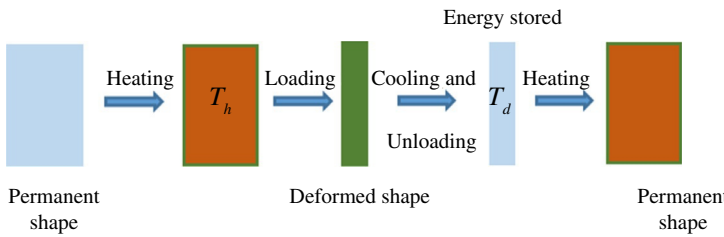

Fig. 7.1 Cycle of SMPs. Thermomechanical cycle of SMPs. No permission required.

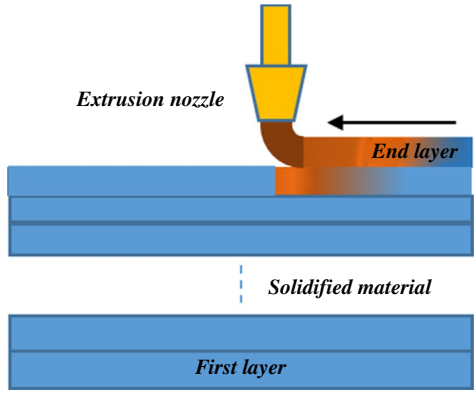

Fig. 7.2 3D Printing technology. Schematic of 3D printing technology. No permission required.

in the liquefier, which is higher than the glassy temperature. So, the nozzle, by applying the force into the filament, extrudes the filament onto the base (called platform or table) and simultaneously prints it on the platform with printing speed S_p. In this step, the filament is heated and stretched, so this step of the printing process is similar to the heating-loading process in the SMP programming, in which the prestrain is created in the sample. By increasing the printing speed, the filament stretches with a greater force; hence, the amount of prestrain induced in the sample is greater. After deposition, the printed layer cools and solidifies in the same way as the cooling step in the programming process. When one layer is printed, the platform moves down, and the printing nozzle moves to build the next layer. Finally, the thermomechanical programming process is completed when the 3D-printed sample is detached from the platform.

It is noteworthy that during the printing process, layers experience several heating–cooling processes. For example, during the printing of the second layer, the first layer heats up somewhat, so some of its prestrain release; hence, its shape memory effect decreases. In such a way, other layers undergo partial heating and some of their prestrain release too. Since the first layer experiences more heating processes, it has lower prestrain than other layers. In the same way, the latest layer does not experience any heating and has the maximum prestrain. The rate of the heating–cooling process plays a significant role in the release of the prestrain. On the contrary, by controlling the printing speed, the rate of the heating–cooling process can be changed. Therefore, the printing speed is one of the critical parameters that can be affected by shape memory programming. For example, at low printing speeds, the sample has more time to cool, so the heating–cooling process slows down, and less amount of prestrain is released. As previously stated, each layer undergoes a different heating–cooling process, resulting in a different amount of induced prestrain in each layer; thus, shape memory programming can be thought of as functionally graded (FG) 4D printing.

Constitutive equations

SMPs are a class of programmable material whose shape changes under external stimuli such as temperature, magnetic, or electric field. Due to the significant development of SMPs and the importance of understanding their complex thermomechanical mechanism, the development of a constitutive equation that is able to predict SMPs behavior is taken into consideration. In this regard, for modeling the SMP mechanism, there are various viewpoints that mainly can be classified as thermoviscoelastic modeling and phase transformation approaches. In this section, these two approaches are described.

Thermoviscoelastic approach

Due to the viscoelastic nature of polymers, thermoviscoelastic modeling can be employed to describe and predict SMP behavior. In this viewpoint, the constitutive equations are based on a rheological model in which the parameters are time and temperature property-dependent. Dashpot, spring, and frictional elements are common components of thermoviscoelastic models. The viscosity is one of the most important features of the SMPs that is due to the mobility between polymer chains, which in such modeling has been considered. Also, in this viewpoint, the modeling predicts SME and predicts the viscoelastic behavior of polymers. Tobushi, Hara, Yamada, and Hayashi (1996) proposed a simple viscoelastic model for investigating SMPs' behavior. In this model, they used a standard linear viscoelastic model (SLV) for modeling the SMP mechanism, in which a Maxwell model is parallel with a spring element. Fig. 7.3 shows the SLV model that consists of three elements.

For the SLV model, the stress–strain relationship can be expressed as follows:

$$\dot{\varepsilon} = \frac{\dot{\sigma}}{E} + \frac{\dot{\sigma}}{\mu} - \frac{\varepsilon}{\lambda} \tag{7.1}$$

where σ and ε show stress and strain, respectively, and E, λ,and μ denote elastic modules, time retardation, and viscosity, respectively.

The SLV model, however, has some limitations, such as a disability in predicting mechanical properties in the glassy transition region and the difference between creep recovery above and below the glass transition region. To settle these issues, they expressed model parameters in the form of an exponential function to solve the drastic

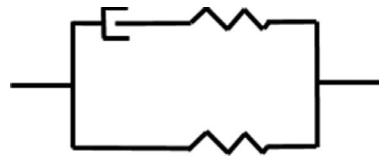

Fig. 7.3 SLV model. The standard linear viscoelastic (SLV) model.
No permission required.

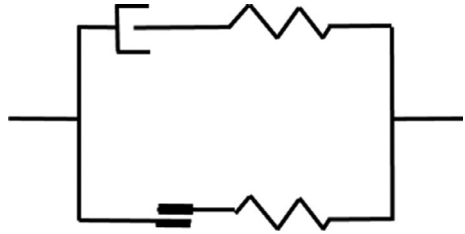

Fig. 7.4 Modified SLV model.
No permission required.

changes in mechanical properties in the glassy region. Also, they added a slip mechanism to solve the difference between creep recovery above and below the glass transition region. Fig. 7.4 shows the modified SLV model.

The stress–strain relationship for the modified SLV model could be expressed as the following equation:

$$\dot{\varepsilon} = \frac{\dot{\sigma}}{E} + \frac{\sigma}{\mu} - \frac{\varepsilon - \varepsilon_s}{\lambda} \tag{7.2}$$

The significant change in mechanical properties of SMPs in the glass transition region could be described as the following form:

$$E = E_g \ exp\left(a_E\left(\frac{T_g}{T} - 1\right)\right) \mu = \mu_g \ exp\left(a_\mu\left(\frac{T_g}{T} - 1\right)\right) \tag{7.3}$$

where E_g and μ_g are the values of E and μ at $T = T_g$.

where E_g and μ_g are the values of E and μ at $T = T_g$, and a_E and a_μ show the slope of straight line.

Phase transformation approach

Polymers are a combination of many chains with different lengths and angles, which each has different entropies and different temperature transitions. During the cooling process, the phase transition first occurs in the chain with lower entropy, so the SMPs have a phase heterogeneity consisting of glassy and rubbery phases. These phases could change into each other under thermal conditions, and during the thermal process, the amount of the changes constantly. By considering the fact that SMPs are a combination of two phases, a new class of constitutive equations was proposed by researchers (Bodaghi et al., 2017). In contrast to the thermoviscoelastic model, or a rheological model, the phase transition model is a phonological model with a physical meaning. These models not only cover the viscosity of the polymers but also predict the phase transformation of SMPs. In this section, one of the phase transition modeling approaches is described.

The volume fraction of glassy and rubbery phases during the thermal process can be expressed by scalar variables ξ_g and ξ_r that can be defined as follows:

$$\xi_g = \frac{V_g}{V}\ \xi_r = \frac{V_r}{V} \tag{7.4}$$

in which V_g shows the volume of the glassy phase and V_r denotes the rubbery-phase volume. Since the SMPs only consist of two phases, rubbery and glassy, the summation of the two phases' volume fractions must be equal to unity ($\xi_g + \xi_r = 1$). The change of the rubbery phase to the glassy phase or vice versa is considered only a function of temperature. Therefore, ξ_g and ξ_r only depend on the temperature, and the volume fraction of the rubbery phase can be rewritten as a function of the glassy volume fraction, as the following form:

$$\xi_r = 1 - \xi_g \tag{7.5}$$

So, the glassy volume and the volume fraction of the glassy phase are independent variables and could be expressed as follows:

$$\xi_g = \xi_g\ (T)\ V_g = V_g\ (T) \tag{7.6}$$

There are different methods to determine mechanical properties. Dynamic mechanical thermal analysis (DMTA) is one of the important tests that determine material properties by considering temperature dependency. In this test, sinusoidal stress is applied to the sample, and its strain is measured. Also, the temperature of the sample changes during the test; therefore, this test can be used to determine temperature-dependent mechanical properties. So, using the DMTA test, the glassy volume fraction can be expressed explicitly as follows:

$$\eta_g = \frac{\tan h\left(a_1 T_g - a_2 T\right) - \tan h\left(a_1 T_g - a_2 T_h\right)}{\tan h\left(a_1 T_g - a_2 T_h\right) - \tan h\left(a_1 T_g - a_2 T_l\right)} \tag{7.7}$$

in which a_i ($i = 1, 2$) are specified by fitting the explicit function on the DMTA curve.

It is assumed that the rubbery and glassy phases in SMPs are linked to each other in series form. Since printed structures are under small deformation and large rotation, the total strain can be written as the sum of four parts; glassy, rubbery, thermal, and inelastic, which is due to phase transformation; Eq. (7.8) shows the total strain:

$$\varepsilon = \xi_g\ \varepsilon_g + \left(1 - \xi_g\right)\ \varepsilon_r + \varepsilon_{in} + \varepsilon_{th} \tag{7.8}$$

where ε shows total strain, and ε_g and ε_r denote strain of the glassy and rubbery phases, respectively; ε_{in} is inelastic strain and ε_{th} represents the thermal strain, which can be defined as an integral part such as the following:

$$\varepsilon_{th} = \int_T^{T_0} \alpha_e\ dT \tag{7.9}$$

in which T_0 expresses the reference temperature and α_e is the equivalent thermal expansion that is dependent on the temperature and defined as follows:

$$\alpha_e = \alpha_r + \left(\alpha_g - \alpha_r\right) \xi_g \left(T\right) \tag{7.10}$$

where α_r and α_g express thermal expansion for rubbery and glassy phases, respectively.

During phase change from rubbery phase to glassy phase, cooling process, the inelastic strain ε_{in}, is stored in the SMP that can be formulated as the following:

$$\dot{\varepsilon}_{in} = \dot{\xi}_g \varepsilon_r \tag{7.11}$$

in which the dot denotes the rating function.

In contrast to the cooling process in which the inelastic strain is stored in the SMPs, in the heating process, the stored strain releases gradually in proportion to the volume fraction of the glassy phase with respect to the preceding glassy phase. The strain storage is expressed as follows:

$$\dot{\varepsilon_{in}} = \frac{\dot{\xi}_g}{\xi_g} \varepsilon_{in} \tag{7.12}$$

In order to derive the stress state, the second law of thermodynamic, the Clausius-Duhem inequality, must be satisfied. The ε and T variables are selected as external control variables, also, ε_g, ε_r, ε_{in},and ξ_g are chosen as internal variables. By considering Helmholtz free energy density functions, stress, σ, can be derived as follows:

$$\sigma = \sigma_g = \sigma_r \tag{7.13}$$

in which the stress of glassy and rubbery phases can be formulated as follows:

$$\sigma_g = C_g \, \varepsilon_g \, \sigma_r = C_r \, \varepsilon_r \tag{7.14}$$

where C is the elasticity tensor which for an isotropic material has two independent constants and defined as follows:

$$C = \frac{E}{(1+\nu)(1-2\nu)} \begin{bmatrix} 1-\nu & \nu & \nu & 0 & 0 & 0 \\ \nu & 1-\nu & \nu & 0 & 0 & 0 \\ \nu & \nu & 1-\nu & 0 & 0 & 0 \\ 0 & 0 & 0 & \frac{1-2\nu}{2} & 0 & 0 \\ 0 & 0 & 0 & 0 & \frac{1-2\nu}{2} & 0 \\ 0 & 0 & 0 & 0 & 0 & 0 \end{bmatrix} \tag{7.15}$$

in which E and ν denote Young's modules and Passion's ratio, respectively. Now by substituting Eq. (7.14) in Eq. (7.8), the stress obtains as follows:

$$\sigma = C_e\ (\varepsilon - \varepsilon_{in} - \varepsilon_{th}) \tag{7.16}$$

where C_e is the equivalent elasticity tensor and expressed with $C_e = (S_r + \xi_g\,(S_g - S_r))^{-1}$, in which S shows the inverse matrix of C ($C = S^{-1}$), the so-called compliance matrix. The stress–strain relationship can be described as follows:

$$\sigma = \left(S_r + \xi_g\ \left(\ S_g - S_r\right)\ \right)^{-1}\ (\varepsilon - \varepsilon_{in} - \varepsilon_{th}) \tag{7.17}$$

In order to solve the nonlinear equation of SMP behavior, it can be considered as an explicit time-discrete stress/strain-temperature-driven problem. The total $[0, t]$ time is broken down into subdomains, and the constitutive equation of SMP is solved in the subdomains $[t^k, t^{k+1}]$. For all variables, the superscript k expresses the value of the variable in the previous step, while the superscript $k+1$ indicates the current step. The inelastic strain expressed with Eqs. (7.18) and (7.19), now by applying the linearized implicit backward Euler integration method to the flow rule, can be discretized as (7.18) and (7.19):

$$\varepsilon_{in}^{k+1} = \varepsilon_{in}^{k} + \Delta\xi_g^{k+1}\ \varepsilon_r^{k+1} \tag{7.18}$$

$$\varepsilon_{in}^{k+1} = \varepsilon_{in}^{k} + \frac{\Delta\xi_g^{k+1}}{\xi_g^{k+1}}\ \varepsilon_{in}^{k+1} \tag{7.19}$$

where

$$\Delta\xi_g^{k+1} = \xi_g^{k+1} - \xi_g^{k} \tag{7.20}$$

By using Eqs. (7.14), (7.17), (7.19), and (7.20) along with a mathematical simplification, we could explicitly update the inelastic strain for the cooling and heating processes. For the cooling process, for stress control, it could be written as follows:

$$\varepsilon_{in}^{k+1} = \varepsilon_{in}^{k} + \Delta\xi_g^{k+1}\ S_r^{k+1}\ \sigma^{k+1} \tag{7.21}$$

and for strain control, it could be written as follows:

$$\varepsilon_{in}^{k+1} = \left(I + \Delta\xi_g^{k+1}\ S_r^{k+1}\ C_e^{k+1}\ \right)^{-1}\ \left(\varepsilon_{in}^{k}\Delta\xi_g^{k}\ S_r^{k+1}\ C_e^{k+1}\ \left(\varepsilon^{k+1} - \varepsilon_{th}^{k+1}\right)\right) \tag{7.22}$$

For the heating process, Eq. (7.22) can be simplified as the following:

$$\varepsilon_{in} = \frac{\xi_g^{k+1}}{\xi_g^k}\ \varepsilon_{in}^k \tag{7.23}$$

Now, by substituting the updated inelastic strain into Eq. (7.17), the stress–strain relationship for heating and cooling processes can be obtained as follows:

$$\sigma^{k+1} = C_D^{k+1}\ \left(\varepsilon^{k+1} - \delta\ \varepsilon_{in}^{k+1} - \varepsilon_{th}^{k+1}\right) \tag{7.24}$$

where elasticity tensor C_D, and the parameter for the heating and cooling processes δ, are defined as follows:

$$\begin{aligned} C_D^{k+1} &= \left(I + \Delta\xi_g^{k+1}\ S_r^{k+1}\ C_e^{k+1}\right)^{-1}\ C_e^{k+1}, \delta = 1\ \dot{T} < 0\ C_D^{k+1} = C_e, \delta \\ &= \frac{\xi_g^{k+1}}{\xi_g^k}\ \dot{T} > 0 \end{aligned} \tag{7.25}$$

Fabrication and modeling 4D-printed elements

Materials

In order to fabricate active elements, the polylactic acid (PLA) has been used as a SMP filament with 1.75 mm diameters and the glass transition temperature of 65°C. In this regard, a 3DGence DOUBLE printer developed by 3DGence has been used, which extrudes a filament 1.75 mm with a $0.4-$ mm nozzle. The 3DGence Slicer software was used to convert the STL file to G-code and control printing parameters. The printing parameters such as the liquefier, chamber, and platform temperatures are set at 210, 24,and 24°C, respectively. The active elements (beam-like elements) were 4D-printed in the shape of a straight beam with the dimension $(30 \times 1.6 \times 1)$ mm for length, width, and thickness, respectively.

One of the most important properties that must be employed in thermomechanical analysis is the dependence of the properties on temperature. Therefore, using a dynamic-mechanical analyzer (DMA, Q800, TA Instruments, New Castle, DE, USA), the temperature-dependent properties for 3D-printed beam-like samples were determined. In this regard, the DMTA test was carried out in the axial tensile mode, in which the frequency of forced oscillation and heating rate were considered 1 Hz and 5°C/min, respectively. Therefore, the results of DMTA 4D-printed beam-like were reported as storage modules, E_s, and phase lag, δ,which is shown in Fig. 7.5. According to the phase lag result, the sample shows its peak curve at 65°C, which indicates the glass transition temperature. It can also be deduced from the diagram of storage modules that at 60°C,the sample experiences a drastic change in its storage modules.

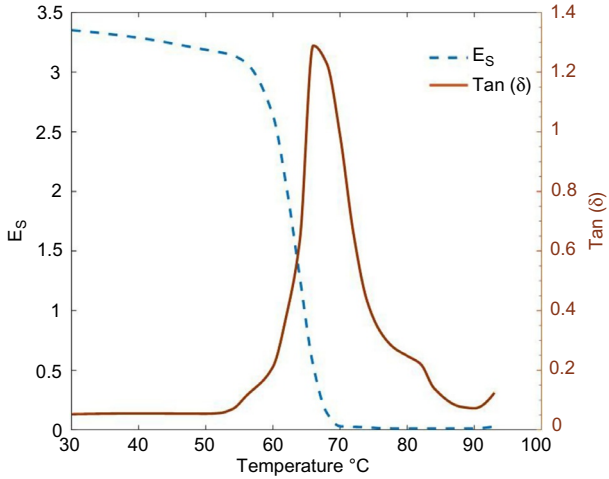

Fig. 7.5 DMA results. The DMA results for 3D-printed PLA.
No permission required.

4D printing elements

As mentioned in the 4D printing programming section, the print speed plays a significant role in inducing the SME on 3D-printed samples. Therefore, five beam-like elements were printed at five different speeds $S_p = 5, 10, 20, 40, 70 \frac{\text{mm}}{\text{s}}$. Fig. 7.6 indicates the straight configuration of the 3D-printed beam-like element. After preparation of the 3D-printed sample, samples were heated by immersion in hot water at a specified temperature of 85°C, which is higher than the glass temperature transition, and then, the samples were placed at room temperature and allowed to cool and reach room temperature (24°C). Fig. 7.7 shows the configuration of the 3D-printed sample after the heating–cooling process. As shown in Fig. 7.7, the straight beam-like element configuration changes to a curved beam under the thermal stimulus. Fig. 7.7A shows the 3D-printed sample, which has been printed at low speed $S_p = 5$ mm/s. In this printing speed, the beam configuration remains unchanged under temperature stimulation,

Fig. 7.6 Straight beam-like configuration. The straight beam-like configuration after 4D printing.
From Noroozi, R., Bodaghi, M., Jafari, H., Zolfagharian, A., & Fotouhi, M. (2020). Shape-adaptive metastructures with variable bandgap regions by 4D printing. *Polymers*, *12*(3), 519. https://doi.org/10.3390/polym12030519.

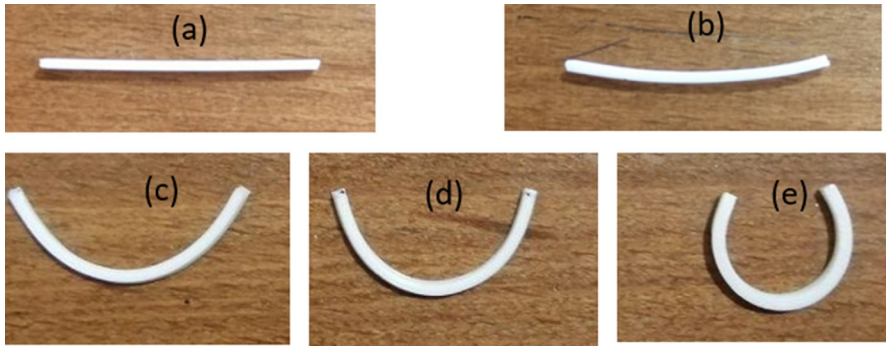

Fig. 7.7 The configuration of the 4D-printed beam-like elements at different speeds. The configuration of the 4D-printed beam-like elements at different speeds of (A) 5, (B) 10, (C) 20, (D) 40, and (E) 70 mm/s after the heating–cooling process.
From Noroozi, R., Bodaghi, M., Jafari, H., Zolfagharian, A., & Fotouhi, M. (2020). Shape-adaptive metastructures with variable bandgap regions by 4D printing. *Polymers*, *12*(3), 519. https://doi.org/10.3390/polym12030519.

and this is because no prestrain has not been induced in the sample. Therefore, the low printing speeds could not be employed in the 4D printing programming. Fig. 7.7B shows the configuration of the sample with print speed $S_p = 10$ mm/s after heating–cooling. In contrast to the previous speed, the beam-like element after the heating–cooling process transforms to a slight curve element at this printing speed, demonstrating that increasing the print speed increases the amount of the induced prestrain. Because of the slight curve at the $S_p = 10$ mm/s, this print speed could be thought of as a transition speed which printed samples with lower than S_p are static elements and higher than are dynamic elements. The self-bending feature is due to the unbalanced prestrain through the sample thickness, in which the lower layer has less prestrain, and the upper layers have more prestrain. As shown in the experiment, by increasing the 4D printing speed, the self-bending/folding feature increases; therefore, by controlling 4D printing speed during the manufacturing process, the shape programming process can be controlled. Nevertheless, the FDM 4D printing technology has high potential in the fabricating and programming active elements with self-bending/folding features.

Finite element modeling

The implementation of constitutive equations in commercial finite element software such as ABAQUS, COMSOL, and ANSYS has been gaining attention due to its extensive application. The constitutive equation of SMPs, due to their complexity, has a lot of difficulties using in finite element software. In this section, to settle this issue by considering the concept of SME and FG 4D printing, a simple method for modeling the thermomechanical behavior of the 4D-printed self-folding element has been proposed. In this regard, the temperature-dependent Young's modulus of the 3D-printed

Table 7.1 Temperature-dependent Young's modulus for 3D-printed PLA.

T (°C)	30	40	50	60	70	80	90
E (*Mpa*)	3350	3280	3166	2554	48	18	14

component has been imported into COMSOL finite element software according to Table 7.1:

As previously stated, the 4D-printed beam-like element can be regarded as an FG material, with the induced prestrain changing gradually along with its thickness. Therefore, to model 4D-printed elements with COMSOL Multiphysics, the sample is divided into multiple sections whose thermal expansion is different. For this purpose, the 4D-printed sample is discretized into six sections. Although considering a large number of sections can lead to a more accurate answer, considering six sections is acceptable in terms of computational cost and accuracy. Fig. 7.8 shows the divided form of a 3D-printed sample in which black and white color shows the first and last printed layers, respectively.

The coefficients of thermal expansion of layers are selected so that the simulated configurations replicate the experimental configurations after the heating–cooling process. Table 7.2 shows the thermal expansion coefficient for different printing speeds.

Considering the obtained coefficients of thermal expansion and applying them into COMSOL finite element software, the beam-like configuration after the heating–cooling process is shown in Fig. 7.9. To describe the geometric features of 4D-printed samples, three parameters are selected, as shown in Fig. 7.9C. The parameters R_1, R_2, and R_3 represent the outer length, opening, and depth length, respectively.

Fig. 7.8 Discretized printed sample. Discretized 4D-printed element.
No permission required.

Table 7.2 The thermal expansion coefficients for different printing speeds.

	S_p (mm/s)			
α_i (1/°C)	**10**	**20**	**40**	**70**
α_1	−0.0006	−0.0016	−0.0018	−0.00252
α_2	−0.0004	−0.0011	−0.0016	−0.00222
α_3	−0.0002	−0.0011	−0.0013	−0.0022
α_4	−0.00009	−0.0008	−0.0011	−0.00172
α_5	−0.00007	−0.0006	−0.0008	−0.00152
α_6	−0.00005	−0.0004	−0.0005	−0.00122

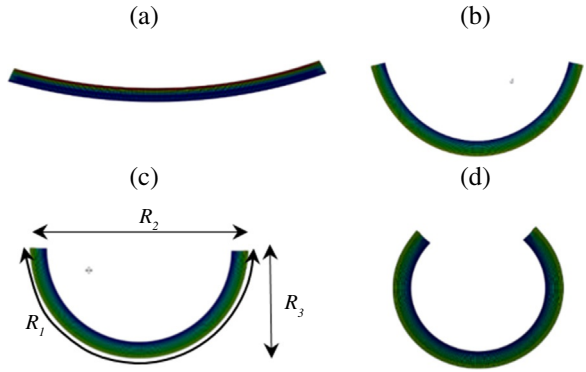

Fig. 7.9 Finite element simulation of the 4D-printed samples. Finite element simulation of the 4D-printed samples for different printing speeds (A) 10, (B) 20, (C) 40, and (D) 70 mm/s after the heating–cooling process.
From Noroozi, R., Bodaghi, M., Jafari, H., Zolfagharian, A., & Fotouhi, M. (2020). Shape-adaptive metastructures with variable bandgap regions by 4D printing. *Polymers*, *12*(3), 519. https://doi.org/10.3390/polym12030519.

As shown in Fig. 7.9, the 4D-printed sample with printing speed, $S_p = 70$ mm/s has much more deformation than other printing speeds, which selected parameters clearly indicate this fact. In addition to the experimental and finite element analysis (FEA), an in-house code for solving the constitutive equation of SMPs is employed. Hence, to investigate the accuracy of the simple method used in the finite element results, the geometric features obtained from experimental, finite element analyses, and in-house code are compared and listed in Table 7.3. As shown in Table 7.3, the in-house code results are consistent with the simple method and experimental results. Therefore, the simple method accuracy and efficiency for the 4D-printed sample with the self-folding feature are validated.

Table 7.3 The geometric parameters of the 4D-printed active element after the heating–cooling process.

Method	S_p (mm/s)	R_1 (mm)	R_2 (mm)	R_3 (mm)
Experiment	10	29.8	28.2	3.1
	20	29.3	19	8.3
	40	29.1	16.3	9.2
	70	29.0	7.1	10.5
In-house FE method	10	29.9	28.3	3.0
	20	29.1	19.2	8.4
	40	29.4	16.3	9.2
	70	29.2	7.2	10.3
FE COMSOL Multiphysics	10	29.7	28.3	3.2
	20	29.4	19.1	8.4
	40	29.2	16.2	9.1
	70	28.9	7.0	10.4

Case studies

In this section, using 4D-printed beam-like elements, which in the previous sections were fabricated and modeled in the finite element software, some of the 4D printing applications have been shown. First, a soft actuator under thermal stimulus is fabricated and modeled. Second, the 4D-printed composites with self-assembly and self-folding features are investigated. Finally, by using passive and active elements, adaptive metastructures with variable bandgap regions are proposed.

Self-folding structures

Self-folding is one of the most important mechanisms that provide the range of motion and changing configuration in nature. The self-folding structure can be used for a wide range of applications such as deployable biomedical devices and self-assembling robots due to their excellent features, including reducing time and effort to assemble complex structures and remote and spontaneous performances. The SMPs are good candidates for being employed in self-folding structures due to their unique properties, such as sensitivity to environmental changes (Felton et al., 2013; Mao et al., 2015). In this section, by employing the 4D-printed beam-like elements, different patterns of self-folding/twisting structures are designed, and their behavior under thermal stimulus has been investigated.

Gripper actuator

The design and fabrication of a practical gripper play an important role in robot performance which leads to overcome robot inaccuracy and enhance overall system performance (Honarpardaz, Tarkian, Ölvander, & Feng, 2017). Therefore, the design and fabrication of various grippers with different patterns and applications have been considered by researchers. In this subsection, by employing the fabricated active beam-like elements, a smart gripper is designed in which four active elements are connected to a passive pyramid. Fig. 7.10 shows the configuration of the gripper before the heating–cooling process. After modeling the gripper in finite element software, it

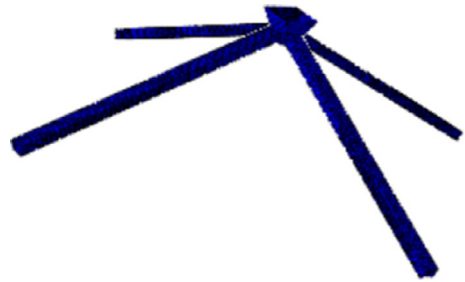

Fig. 7.10 Gripper configuration. Gripper configuration before the heating–cooling process. No permission required.

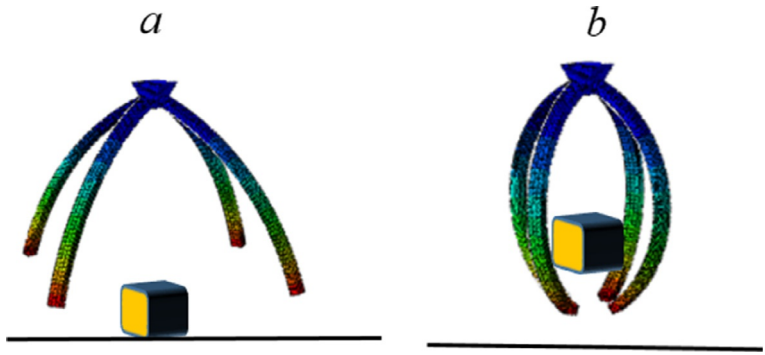

Fig. 7.11 The gripper deformed configuration. The FE Abaqus simulation of the gripper at printing speed: (A) 20 and (B) 40 mm/s.
No permission required.

is exposed to external heat, and its temperature reaches 65 °C and then cooled down to the temperature room. Fig. 7.11 represents the deformed configuration of the gripper. As shown in Fig. 7.11, due to the self-folding feature of active elements, the gripper after thermal stimulus exhibits a self-folding behavior so that it can be used as a soft robotic gripper. The amount of bending angle can be tuned by changing printing speed. For instance, beam-like components with higher 4D printing speeds have more bending angles, and as a result, the various deformed configurations can be achieved by controlling the printing speed, which makes it possible to work in different situations.

Self-folding smart composites

There are different strategies to generate a self-folding mechanism. One of them that during the last decades has been considered by researchers is the embedded rigid particles in the soft matrix and controlling their orientation (Schmied, Le Ferrand, Ermanni, Studart, & Arrieta, 2017; Sydney Gladman, Matsumoto, Nuzzo, Mahadevan, & Lewis, 2016; Wang et al., 2018). One of the critical parameters that significantly affect the controllability of composite deformation is rigid particle orientation. To address this issue, rigid particles can be replaced with continuous fiber to gain better controllability. In this subsection, using the active elements, three patterns of self-folding smart composites are designed and modeled.

In the first pattern, a self-assemble structure is created using 4D-printed elements. In this regard, a flat paper sheet is reinforced with eight 4D-printed elements. Fig. 7.12 shows the undeformed configuration of the self-assemble structure. In order to predict the thermomechanical behavior of the self-assemble structure under the thermal stimulus, the simple method is employed in the finite element software. According to the DMTA test, PLA has a low Young's modulus at 85 °C. Therefore, if the active elements are heated up to 85 °C, the stiffness of the paper prevents elements from deformation and backs them to their straight configuration. To solve this issue, in the FEM, the structure is heated up to 65 °C. The interaction between 4D-printed elements and

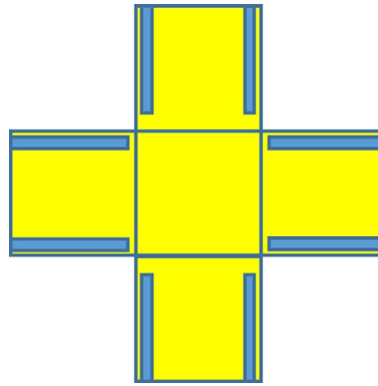

Fig. 7.12 Configuration of the smart composite. Configuration of the smart composite before the heating–cooling process.
No permission required.

the paper sheet is considered perfect bound, in which there is no relative displacement among them. The heating–cooling process is applied to the structure so that at first, the structure is heated up to 65 °C and then cooled to room temperature. Fig. 7.13 indicates the deformed self-assemble configuration after the heating–cooling process.

As shown in Fig. 7.13, the self-assembly structure's deformation, with the initial flat state form, can be considered a 2D-to-3D shape changing, which can be called a self-assembly mechanism. By increasing the printing speed, the structure undergoes more bending so that the printing speed of $S_p = 70$ mm/s has more bending, and on the contrary, the speed of $S_p = 20$ mm/s has the least bending. It should be noted that in to have the best self-assemble structure, the optimum printing speed should be used, in

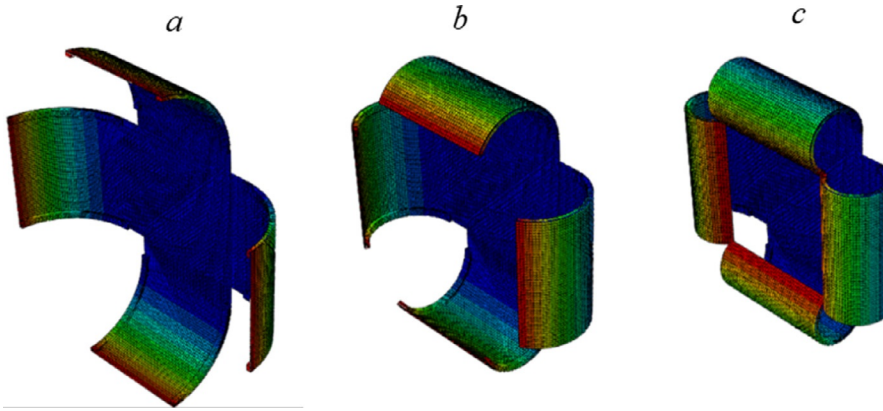

Fig. 7.13 Simulated configuration of the self-assembly composite. The simulated configuration of the self-assembly composite after the heating–cooling process for (A) 20, (B) 40, and (C) 70 mm/s.
No permission required.

Fig. 7.14 The hand-like gripper. Undeformed configuration of the hand-like gripper. No permission required.

which in this structure the printing speed of $S_p = 40$ mm/s is optimum printing speed. Also, by changing the arrangement of 4D-printed elements along the flat paper sheet, different self-assembly patterns can be obtained.

As a second pattern, a smart hand-like structure is proposed in which a hand-like flat paper sheet is reinforced with 4D-printed elements. Fig. 7.14 shows the undeformed configuration of the hand-like structure. To model the thermomechanical behavior of the hand-like structure, the proper thermal and mechanical boundary conditions are applied to the FEM. For this purpose, it is assumed that the interaction between 4D-printed elements and the paper sheet is tie-type, which means there is no relative motion between them. Also, the structure is heated up to 65 °C and then cooled to room temperature. Fig. 7.15 represents the configuration of the hand-like structure after the heating–cooling process for three different printing speeds. As shown, the active elements bend under the thermal stimulus, and as a result, the shape of the hand-like structure changes under the thermal stimulus. Also, different printing speeds have different bending angles, which indicates the potential of printing speeds to generate wide ranges of hand motion patterns.

The third pattern is a smart corrugated structure that is reinforced with horizontal 4D-printed elements, which are attached to both paper sides. Fig. 7.16 shows its undeformed configuration at the top and cross-sectional view, in which the yellow elements show the 4D-printed element attached upward and the black line shows the bottom 4D-printed elements. The attachment between paper sheer and elements is that the first printed layer is connected to the paper. For modeling the thermomechanical behavior of the 4D-printed elements, the variable coefficient thermal expansion technique has been employed in finite element software. The thermal and mechanical boundary conditions are tie-type and 65 °C, respectively. After the heating up structure to 65 °C, it is placed at a specific temperature (room temperature) to cool down. Fig. 7.17 represents the deformed configuration of the rectangular structure after the

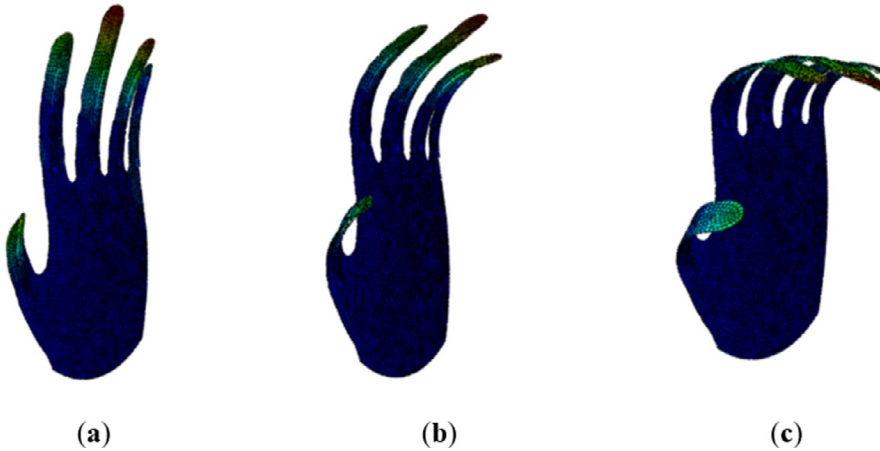

Fig. 7.15 The deformed configuration of the hand-like gripper. The deformed configuration of the hand-like gripper after heating–cooling process for (A) 20, (B) 40, and (C)70 mm/s.
No permission required.

Fig. 7.16 Configuration of the smart corrugated structure. Configuration of the smart corrugated structure with horizontal 4D-printed beams.
No permission required.

heating–cooling process for three different speeds. After applying an external stimulus, the 2D reinforced rectangular paper wrinkles to form a 3D corrugated structure. As shown, different printing speeds have different pitches, so the higher the printing speed, the lower the pitch value. Moreover, one of the parameters that significantly affect the corrugated feature is the distance between 4D-printed elements.

Adaptive dynamic structures

One of the most important issues in our modern daily life is the analysis of acoustic waves. Acoustic metamaterials are a type of architect material that is designed to control and manipulate waves passing through it. The periodic structures as a kind of metamaterials have the ability to damp some specific frequency ranges of elastic waves, called bandgap or stopband (Bertoldi & Boyce, 2008; D'Alessandro, Zega, Ardito, & Corigliano, 2018; Li, Wang, & Yan, 2021; Meaud & Che, 2017). In other words, while elastic wave propagation occurs in all directions in the propagating frequency ranges, bandgap areas provide a frequency range where elastic wave propagation is stopped, and this ability can be used in a variety of applications, including controlling and managing wave propagation and acoustic mirrors. The geometry and material type of periodic structure determine the bandgap width, frequency level, and modal location of the structure (D'Alessandro et al., 2018).

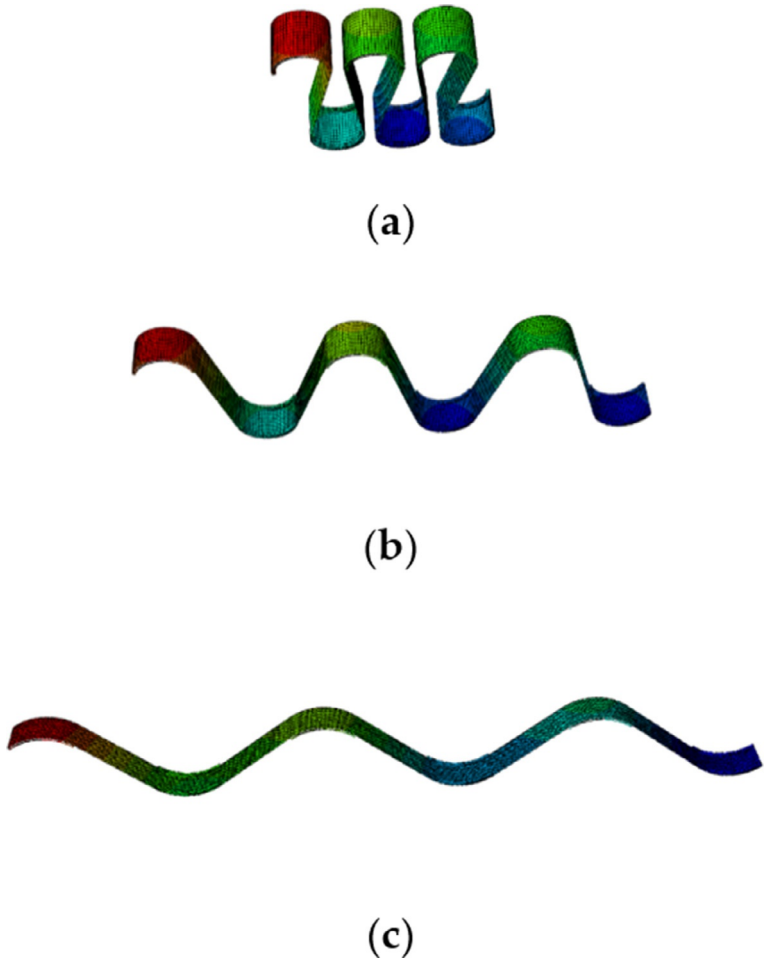

Fig. 7.17 The FE simulated smart corrugated structure. The FE-simulated smart corrugated structure after the heating–cooling process: (A) 20, (B) 40, and (C)70 mm/s.
No permission required.

Traditional materials and structures do not change their configuration and properties, so they can only be used in a constant range of frequency. The researchers have designed adaptive structures with variable and uncommon behavior in different applications. Therefore, by employing different methods, researchers have tried to design and fabricate adaptive and tunable structures (Bertoldi & Boyce, 2008; Bertoldi, Boyce, Deschanel, Prange, & Mullin, 2008; D'Alessandro et al., 2018; Li et al., 2021; Li, Wang, Chen, Wang, & Bao, 2019; Meaud & Che, 2017; Shim, Wang, & Bertoldi, 2015; Singh & Pandey, 2018).

Wave propagation formulation

To study wave propagation in architected period structures, the Bloch theorem has been used. Based on the Bloch theorem, the displacement of any point in a periodic architected structure can be defined as a function of the displacement of its corresponding point in the reference unit cell ($\vec{U}_{Ref}\left(\vec{r}\right)$). As a result, wave propagation analyses for the entire periodic structure were simplified to solve equations for a unit cell.

Where $\vec{U}\left(\vec{r},t\right)$ expresses displacement for an arbitrary point in the periodic structure and $\vec{U}_{Ref}\left(\vec{r}\right)$ indicates its corresponding point in the reference unit cell. Also, $\vec{R}$ and $\vec{r}$ show the lattice and position vector, respectively. Besides, $\vec{k} = (k_1, k_2)$ is the wave vector and k_1 and k_2 are its components along the x and y directions, respectively. Also, ω and t indicate frequency and time, respectively. In order to define periodically in the period structures, the direct vector must be specified. Fig. 7.18 shows a periodic structure in which a_1 and a_2 are direct vectors that according to them, the lattice vector defines as follows:

$$\vec{R} = n_1\,\vec{a}_1 + n_2\,\vec{a}_2\; n_1, n_2 = 0, \pm 1, \pm 2, \ldots \tag{7.26}$$

Bloch wave vector varies in the Brillouin zone. Therefore, to analyze the wave propagation, the reciprocal space corresponding to the direct space should be defined, which is shown in the following equation.

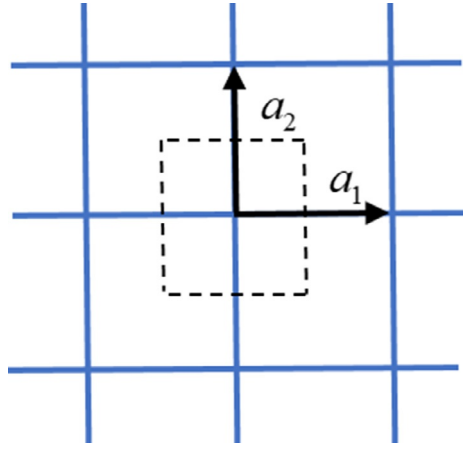

Fig. 7.18 Direct vectors of periodic structure. Periodic structure with its direct vectors. No permission required.

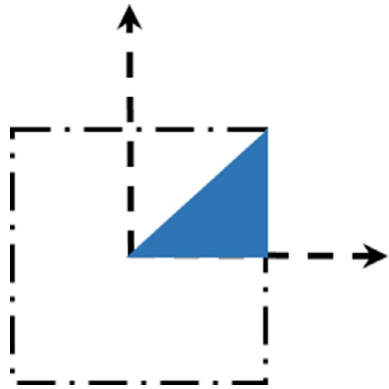

Fig. 7.19 First Brillouin zone and irreducible Brillouin zone. First Brillouin zone (FBZ, dashed square) and irreducible Brillouin zone (IBZ, colored triangle).
No permission required.

$$\vec{a}_i.\vec{b}_j = 2\pi\,\delta_{ij} = \begin{cases} \vec{b}_1 = 2\pi \dfrac{a_2 \times a_3}{a_1.(a_2 \times a_3)} \\ \vec{b}_2 = 2\pi \dfrac{a_3 \times a_1}{a_1.(a_2 \times a_3)} \end{cases} a_3 = (0,0,1) \tag{7.27}$$

where δ_{ij} is the Kronecker delta.

Fig. 7.19 shows the first Brillouin zone (FBZ) and irreducible Brillouin zone (IBZ). To analyze the wave propagation, the IBZ has been employed which is a small part of the FBZ (Fig. 7.19).

According to the equation just now mentioned, the wave propagation is a linear eigenvalue problem with three unknown parameters ω, k_1, and k_2 which the wave vector investigates in the IBZ. To solve the wave propagation equations, COMSOL Multiphysics software is employed. Also, convergence studies on mesh size have been performed to achieve reliable and accurate results.

Design adaptive periodic structures

In this section, using the concept of active and passive elements, two periodic structures are conceptually proposed. The term passive elements imply elements that under thermal stimulus do not change their configuration and dynamic behavior. As mentioned in the previous sections, 4D-printed beam-like elements during the printing process can be programmed to show a dynamic behavior under the stimulus. No induced prestrain is generated in the 4D-printed sample at low printing speeds. Therefore, low printing speeds, such as 5 mm/s, can be used to print passive elements. On the contrary, active elements are printed at a high printing speed, in which the induced prestrain is generated along with the sample and under the thermal stimulus changes its dynamic behavior and shows self-folding features. Therefore, by employing active and passive elements and arranging them into a periodic structure, two architected

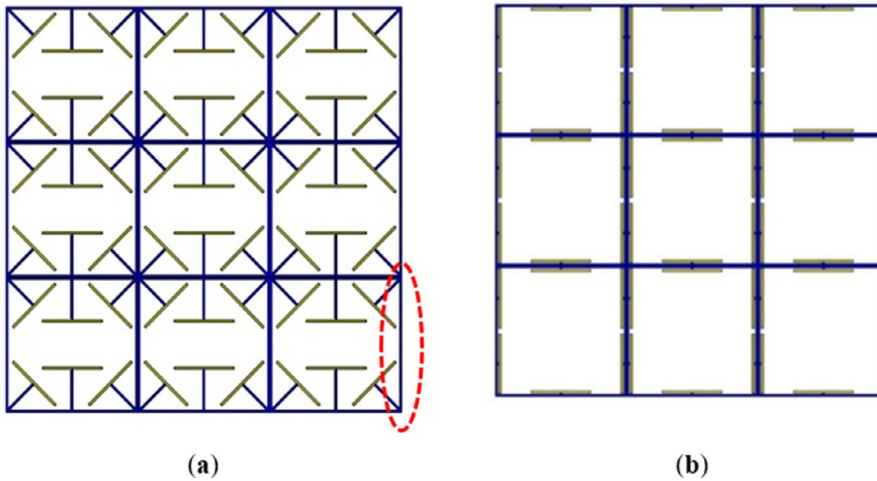

Fig. 7.20 Periodic adaptive structures. Periodic adaptive structures with active and passive elements: (A) diagonal structure and (B) parallel structure (the *dashed line* shows the fixed-fixed beam which is used for the frequency normalization).
From Noroozi, R., Bodaghi, M., Jafari, H., Zolfagharian, A., & Fotouhi, M. (2020). Shape-adaptive metastructures with variable bandgap regions by 4D printing. *Polymers*, *12*(3), 519. https://doi.org/10.3390/polym12030519.

structures have been designed. Structures consist of a mainframe and beam-like elements, which are made of passive and active elements, respectively. The first arrangement is such that the active elements in the diagonal and parallel form are connected to the passive frame. The second arrangement is such that the active elements are connected in parallel to the passive frame. In order to simplify, the first and second structures are called diagonal and parallel, respectively. Fig. 7.20 represents the designed periodic adaptive structure, in which yellow and blue colors indicate active and passive elements, respectively.

Adaptive diagonal structure

The wave propagation properties in the terms of dispersion curve of adaptive diagonal structures are studied. In this section, COMSOL-based numerical have been used to show how adaptive periodic structures can be designed with variable dynamic performance without adding additional resonant components.

To ensure the accuracy of results, the bandgap of a triangular structure was calculated and compared with the earlier results (Srikantha Phani, Woodhouse, & Fleck, 2006). As shown in Fig. 7.21, the COMSOL-based results are in good agreement with the earlier results, which indicates the accuracy of the method used in the COMSOL Multiphysics software.

Eigenfrequencies of adaptive periodic structures are calculated by applying periodic boundary conditions to different elastic wave vectors estimated based on the IBZ. The first natural frequency of the fixed-fixed beam, shown in Fig. 7.20 with a

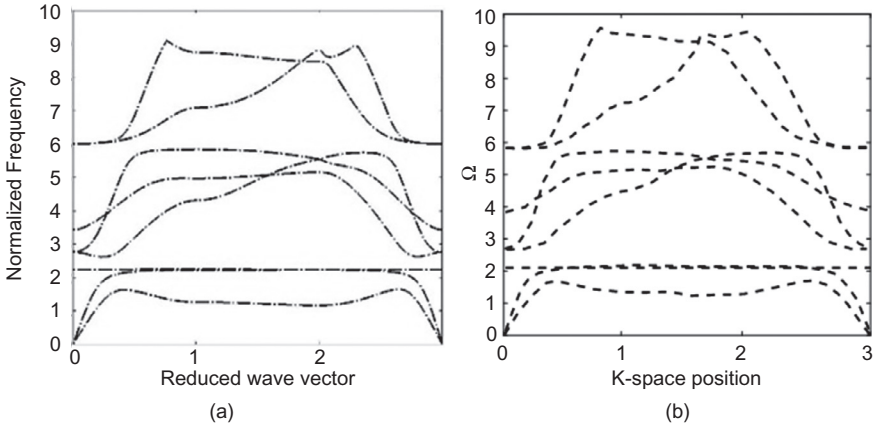

Fig. 7.21 Results validations. Comparison of COMSOL-based results with.
From Noroozi, R., Bodaghi, M., Jafari, H., Zolfagharian, A., & Fotouhi, M. (2020). Shape-adaptive metastructures with variable bandgap regions by 4D printing. *Polymers*, *12*(3), 519. https://doi.org/10.3390/polym12030519.

dashed line, is used to normalize eigenfrequencies in the form of $\Omega = {}^{\omega}/_{\omega_0}$, in which $\omega_0 = 22.4\sqrt{{}^{EI}/_{mL_0^4}}$ expresses the first natural frequency of the fixed-fixed beam.

Fig. 7.22 represents dispersion curves and some of the mode shapes for diagonal structure before any external stimulus. It can be seen from the dispersion curves that there is a bandgap in the range of 1.902 to 2.043, which is shown in gray color. This bandgap region covers 4.68% of the total frequency range. By considering the mode shapes, it is determined that the cause of the bandgap is the resonation of active elements.

After stimulating the diagonal structure under the heating–cooling process, the active element shows their self-bending features and changes mass distribution and stiffness in the structures. Fig. 7.15 shows the changed configuration for three different printing speeds. As shown in Fig. 7.23, the structure with a higher 4D printing speed undergoes more change, and its 4D-printed elements have more curvature and deformation. Fig. 7.24 shows the dispersion curves for the diagonal structure at different printing speeds. The bandgap area for the print speed of 20 m/s is in the range of 1.751 to 2.043, which covers 4.68% of the total frequency range. For the print speed of 40 m/s (Fig. 7.25), the bandgap area covers $\Omega = 1.751$ to 1.812 of the frequency range, which covers a smaller range of the total frequency than the print speed of 20 m/s. Unlike the previous two print speeds, at a print speed of 70 m/s (Fig. 7.26), there is no bandgap area in the frequency range. The obtained dispersion curves for different printing speeds show that using 4D-printed elements can achieve adaptive structures which keep their performance in the various functional ranges.

The dispersion curves obtained from two printing speeds of 20 and 40 m/s indicate increasing printing speed has a little effect on bandgap width and only moves the

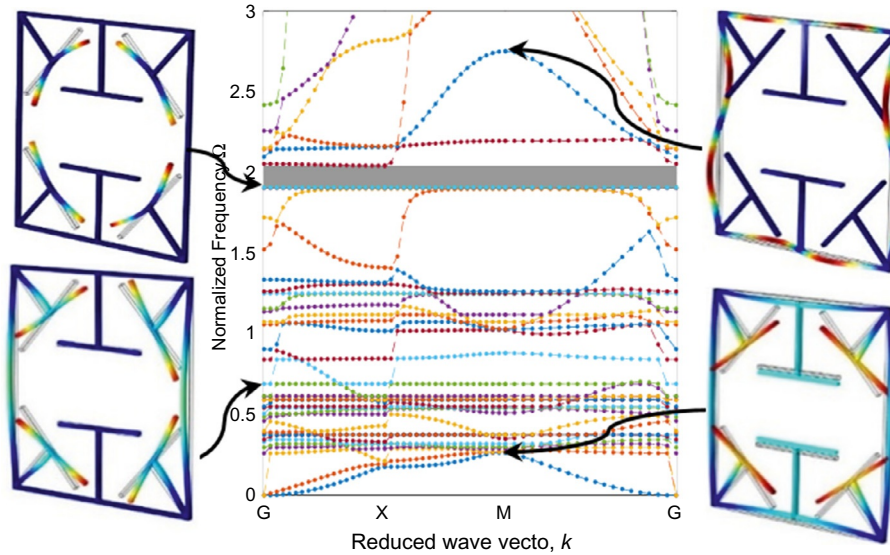

Fig. 7.22 Dispersion of the diagonal metastructure. Dispersion curves and mode shapes of the diagonal metastructure.
From Noroozi, R., Bodaghi, M., Jafari, H., Zolfagharian, A., & Fotouhi, M. (2020). Shape-adaptive metastructures with variable bandgap regions by 4D printing. *Polymers*, *12*(3), 519. https://doi.org/10.3390/polym12030519.

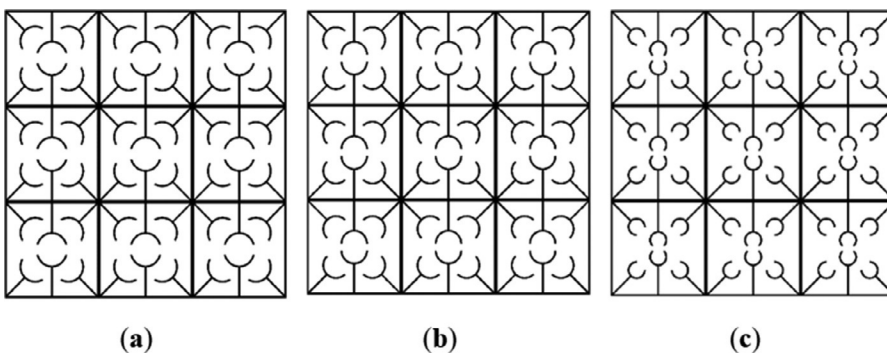

Fig. 7.23 The deformed configuration of the adaptive periodic diagonal structure. The deformed configuration of the adaptive periodic diagonal structure after the heating–cooling process for three different 4D printing speeds: (A) 20, (B) 40, and (C) 70 mm/s.
From Noroozi, R., Bodaghi, M., Jafari, H., Zolfagharian, A., & Fotouhi, M. (2020). Shape-adaptive metastructures with variable bandgap regions by 4D printing. *Polymers*, *12*(3), 519. https://doi.org/10.3390/polym12030519.

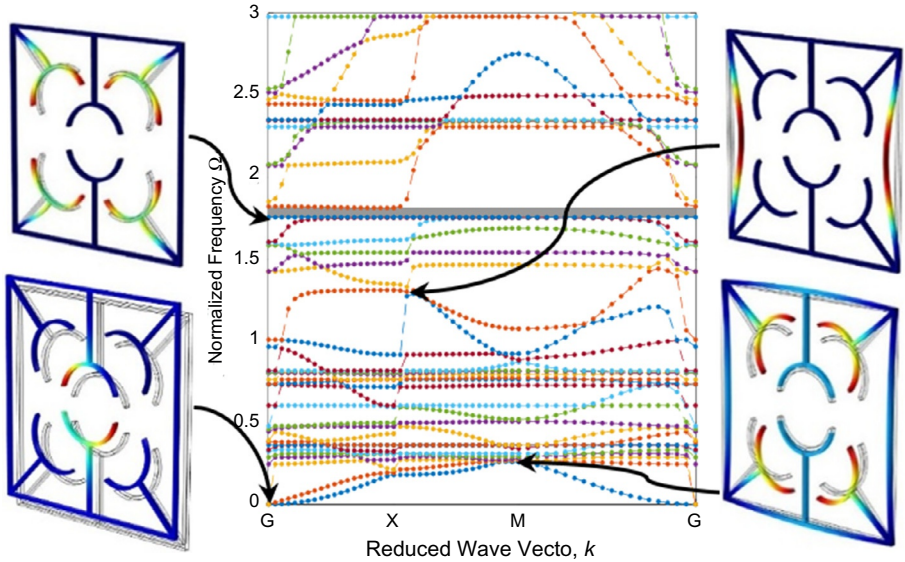

Fig. 7.24 Dispersion curves and mode shapes of the diagonal structure for printing speed 20 mm/s. Dispersion curves and mode shapes of the diagonal structure with the 4D printing speed at 20 mm/s after the heating–cooling process.
From Noroozi, R., Bodaghi, M., Jafari, H., Zolfagharian, A., & Fotouhi, M. (2020). Shape-adaptive metastructures with variable bandgap regions by 4D printing. *Polymers*, *12*(3), 519. https://doi.org/10.3390/polym12030519.

stopband region. However, increasing the print speed does not always change the stopband range. For example, when the printing speed increases to 70 mm/s, the bandgap region vanishes, and the structure transmits the whole wave in all frequency ranges. In general, the results show that by changing 4D printing speeds, different dispersion curves can be obtained, which by manipulating the appropriate and functional bandgap region can be found. Hence, the 4D printing elements have a high potential to fabricate adaptive structures with variable bandgap regions.

Adaptive parallel structure

As mentioned in the previous section, in the parallel structure, the active elements are connected to the passive frame in parallel. Fig. 7.27 shows the dispersion curves for parallel structures before any heating–cooling process. The dispersion behavior for parallel structures is different from the diagonal structure. As shown in dispersion curves, unlike the diagonal structure in which the bandgap region appears in the frequency range, no bandgap region has not appeared, and the whole elastic wave in the range of 1–3 passes through the structure. Fig. 7.28 indicates the parallel structure configuration after the heating–cooling process for three 4D printing speeds. As expected, the 4D-printed active elements under thermal stimulus change their configuration and activate their self-bending features. Hence, by changing the configuration

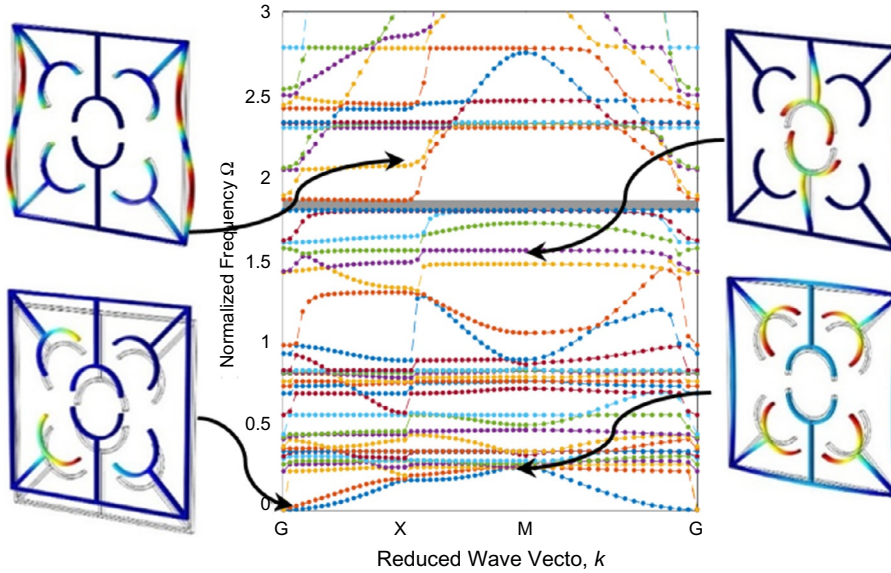

Fig. 7.25 Dispersion curves and mode shapes of the diagonal structure for printing speed 40 mm/s. The counterpart of Fig. 7.12 for 40 mm/s.
From Noroozi, R., Bodaghi, M., Jafari, H., Zolfagharian, A., & Fotouhi, M. (2020). Shape-adaptive metastructures with variable bandgap regions by 4D printing. *Polymers*, *12*(3), 519. https://doi.org/10.3390/polym12030519.

of structures, the mass distribution and stiffness of the structure change, and as a result, dynamic behaviors change. Figs. 7.29–7.31 show the dispersion curves and mode shapes of the parallel structure after the heating–cooling process for different printing speeds of 20, 40, and 70 m/s, respectively.

After the heating–cooling process, the 4D-printed beam-like elements change their configuration to a bent state. As shown in the dispersion curves, after the heating–cooling process, the parallel structure printed at a speed of 20 m/s, a narrow region of bandgap in the range of 1.945 to 1.989 appears in dispersion curves. The ratio of the bandgap range to the total frequency range is 1.48%. By changing the printing speed to 40 mm/s, the beam-like elements bend, and as a result, the dispersion curves change. At this printing speed, multiple bandgap regions appear in the dispersion curve. The multiple ranges of bandgap regions are in the range of 2.172 to 2.231, 2.371 to 2.505, 2.421 to 2.430, 2.441 to 2.569, and 2.594 to 2.765, which in the practical view has more performance than other structures and covers 12.32% of the total frequency range. The printed structure, at a printing speed of 70 m/s, does not experience any bandgap region, and all of the elastic waves pass through the structure. By considering the parallel structure dispersion curves, it could be concluded that the parallel structure shows a better performance than the diagonal structure. The parallel structure covers more and multiple bandgap regions so that it locally resonates filters in the broader range.

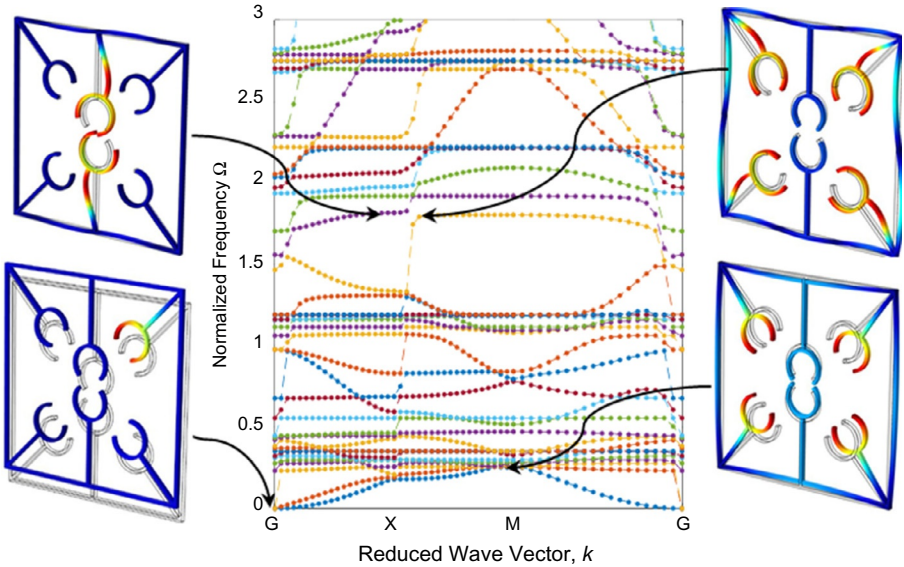

Fig. 7.26 Dispersion curves and mode shapes of the diagonal structure for printing speed 70 mm/s. The counterpart of Fig. 7.12 for 70 mm/s.
From Noroozi, R., Bodaghi, M., Jafari, H., Zolfagharian, A., & Fotouhi, M. (2020). Shape-adaptive metastructures with variable bandgap regions by 4D printing. *Polymers*, *12*(3), 519. https://doi.org/10.3390/polym12030519.

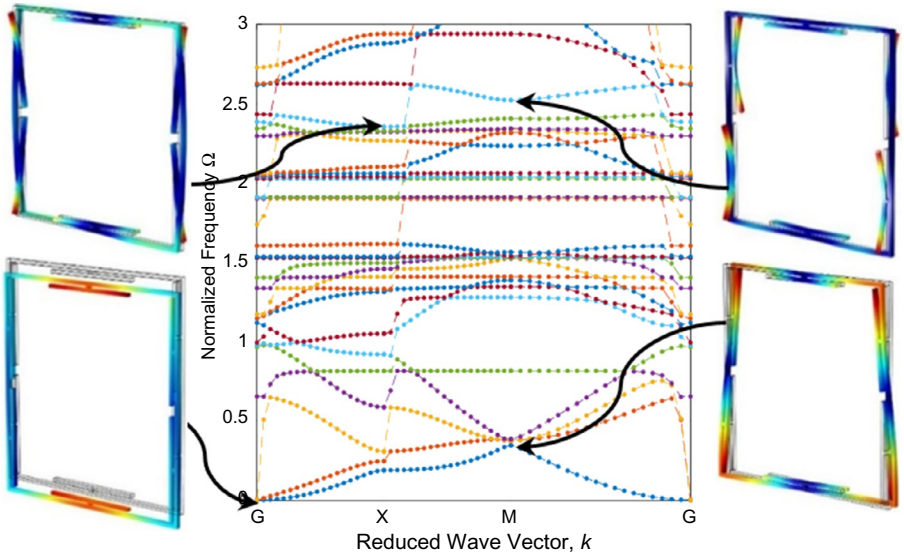

Fig. 7.27 Dispersion curves and mode shapes of the adaptive parallel structure. Dispersion curves and mode shapes of the adaptive parallel structure.
From Noroozi, R., Bodaghi, M., Jafari, H., Zolfagharian, A., & Fotouhi, M. (2020). Shape-adaptive metastructures with variable bandgap regions by 4D printing. *Polymers*, *12*(3), 519. https://doi.org/10.3390/polym12030519.

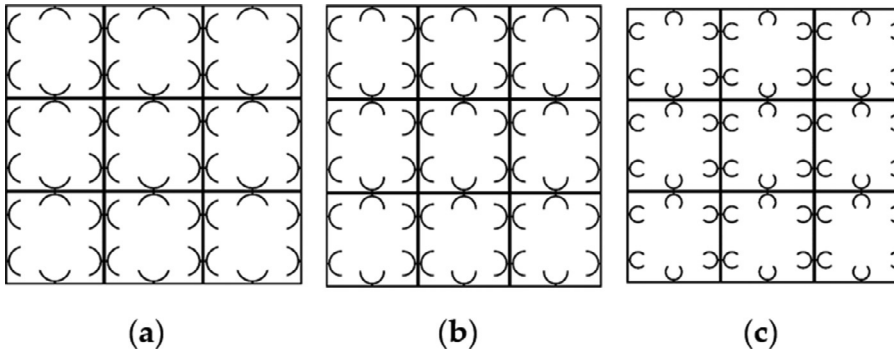

Fig. 7.28 The deformed configuration of the adaptive periodic parallel structure. The deformed configuration of the adaptive periodic parallel structure after the heating–cooling process for three different 4D-printing speeds: (A) 20, (B) 40, and (C) 70 mm/s.
From Noroozi, R., Bodaghi, M., Jafari, H., Zolfagharian, A., & Fotouhi, M. (2020). Shape-adaptive metastructures with variable bandgap regions by 4D printing. *Polymers*, *12*(3), 519. https://doi.org/10.3390/polym12030519.

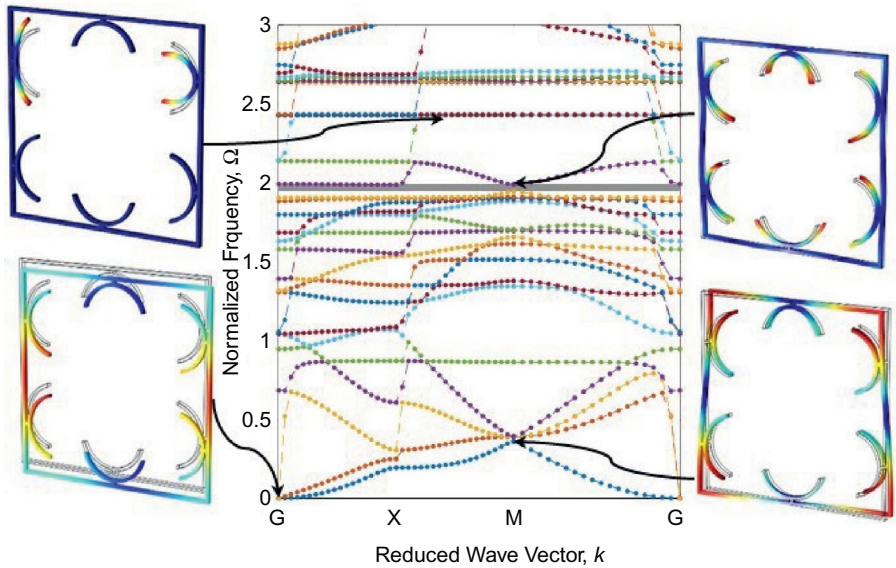

Fig. 7.29 Dispersion curves and mode shapes of the adaptive parallel structure for printing speed 20 mm/s. Dispersion curves and mode shapes of the adaptive parallel structure with 4D-printed active elements at 20 mm/s after the heating–cooling process.
From Noroozi, R., Bodaghi, M., Jafari, H., Zolfagharian, A., & Fotouhi, M. (2020). Shape-adaptive metastructures with variable bandgap regions by 4D printing. *Polymers*, *12*(3), 519. https://doi.org/10.3390/polym12030519.

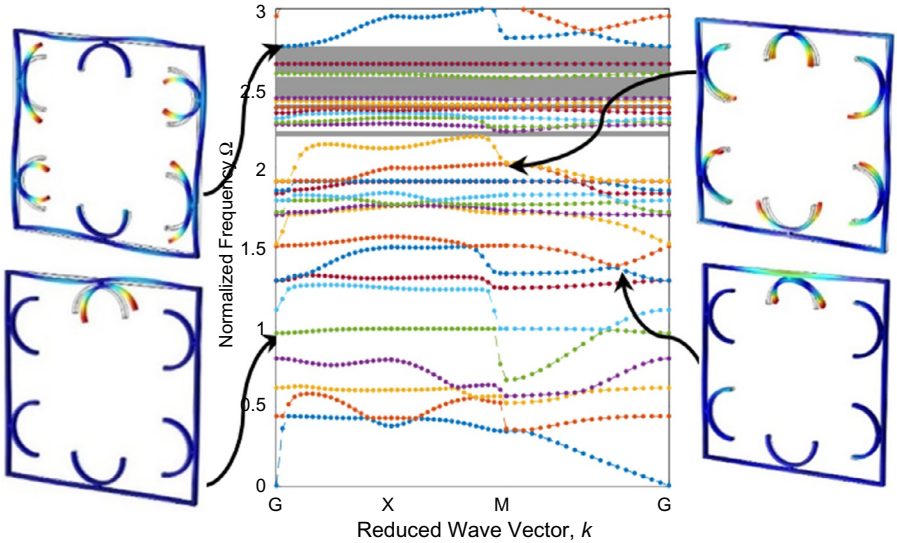

Fig. 7.30 Dispersion curves and mode shapes of the adaptive parallel structure for printing speed 40 mm/s. The counterpart of Fig. 7.17 for 40 mm/s.
From Noroozi, R., Bodaghi, M., Jafari, H., Zolfagharian, A., & Fotouhi, M. (2020). Shape-adaptive metastructures with variable bandgap regions by 4D Printing. *Polymers*, *12*(3), 519. https://doi.org/10.3390/polym12030519.

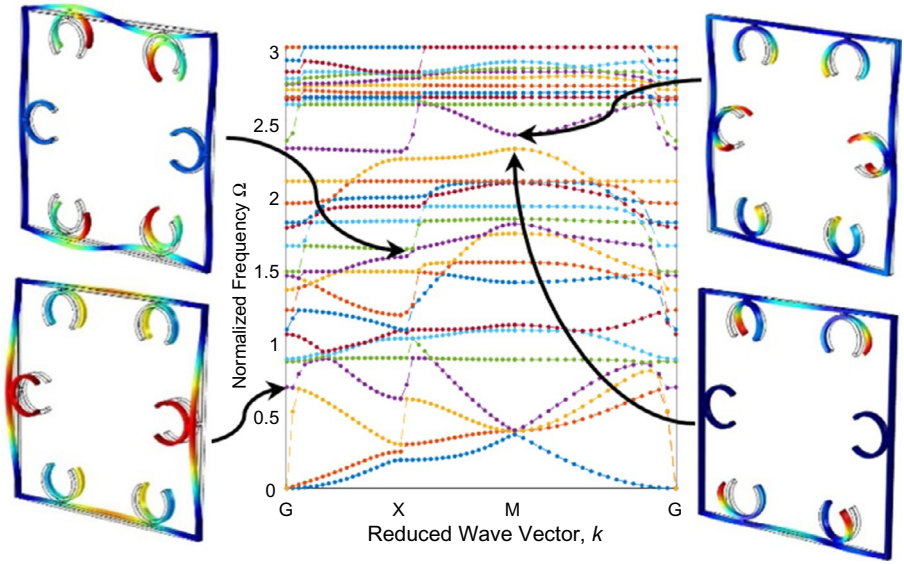

Fig. 7.31 Dispersion curves and mode shapes of the adaptive parallel structure for printing speed 70 mm/s. The counterpart of Fig. 7.17 for 70 mm/s.
From Noroozi, R., Bodaghi, M., Jafari, H., Zolfagharian, A., & Fotouhi, M. (2020). Shape-adaptive metastructures with variable bandgap regions by 4D printing. *Polymers*, *12*(3), 519. https://doi.org/10.3390/polym12030519.

Conclusion

In this chapter, first, the constitutive equations of SMPs based on the thermoviscoelastic and phase transformation approach were introduced. Then, by employing FDM technology, one of the most popular 3D printing methods, the concept of 4D printing technology was presented. It was shown, experimentally, that during the 3D printing technology, the sample is subjected to a thermomechanical cycle similar to shape memory programming. Moreover, it was shown that printing speed has many effects on the 3D-printed sample shape memory effect. Due to the importance of modeling the thermomechanical behavior of 4D-printed samples, based on the concept of FG 4D printing, simple to reproduce but the accurate method was presented to predict 4D-printed sample behavior. This method was validated and calibrated with experimental results and correctly predicted the self-folding feature of 4D-printed elements. As case studies, the thermomechanical behavior of the smart gripper and self-folding smart composite structures under external stimulus was investigated. Also, by using the 4D-printed elements, the adaptive dynamic structures were designed and modeled in finite element software and their bandgap region were analyzed for different printing speeds.

References

Ahmed, K., Shiblee, M. N. I., Khosla, A., Nagahara, L., Thundat, T., & Furukawa, H. (2020). Recent progresses in 4D printing of gel materials. *Journal of the Electrochemical Society*, *167*, 037563b.

Askari, M., Afzali Naniz, M., Kouhi, M., Saberi, A., Zolfagharian, A., & Bodaghi, M. (2021). Recent progress in extrusion 3D bioprinting of hydrogel biomaterials for tissue regeneration: A comprehensive review with focus on advanced fabrication techniques. *Biomaterials Science*, *9*(3), 535–573. https://doi.org/10.1039/d0bm00973c.

Attaran, M. (2017). The rise of 3-D printing: The advantages of additive manufacturing over traditional manufacturing. *Business Horizons*, *60*(5), 677–688. https://doi.org/10.1016/j.bushor.2017.05.011.

Bertoldi, K., & Boyce, M. C. (2008). Mechanically triggered transformations of phononic band gaps in periodic elastomeric structures. *Physical Review B*. https://doi.org/10.1103/physrevb.77.052105.

Bertoldi, K., Boyce, M. C., Deschanel, S., Prange, S. M., & Mullin, T. (2008). Mechanics of deformation-triggered pattern transformations and superelastic behavior in periodic elastomeric structures. *Journal of the Mechanics and Physics of Solids*, *56*(8), 2642–2668. https://doi.org/10.1016/j.jmps.2008.03.006.

Bodaghi, M., & Liao, W. H. (2019). 4D printed tunable mechanical metamaterials with shape memory operations. *Smart Materials and Structures*, *28*(4). https://doi.org/10.1088/1361-665x/ab0b6b, 045019.

Bodaghi, M., Serjouei, A., Zolfagharian, A., Fotouhi, M., Rahman, H., & Durand, D. (2020). Reversible energy absorbing meta-sandwiches by FDM 4D printing. *International Journal of Mechanical Sciences*, *173*. https://doi.org/10.1016/j.ijmecsci.2020.105451, 105451.

Bodaghi, M., Damanpack, A. R., & Liao, W. H. (2017). Adaptive metamaterials by functionally graded 4D printing. *Materials and Design*, *135*, 26–36. https://doi.org/10.1016/j.matdes.2017.08.069.

Bodaghi, M., Noroozi, R., Zolfagharian, A., Fotouhi, M., & Norouzi, S. (2019). 4D printing self-morphing structures. *Materials*, *12*(8). https://doi.org/10.3390/ma12081353.

Damanpack, A. R., Bodaghi, M., & Liao, W. H. (2020). Contact/impact modeling and analysis of 4D printed shape memory polymer beams. *Smart Materials and Structures*, *29*(8). https://doi.org/10.1088/1361-665x/ab883a, 085016.

D'Alessandro, L., Zega, V., Ardito, R., & Corigliano, A. (2018). 3D auxetic single material periodic structure with ultra-wide tunable bandgap. *Scientific Reports*. https://doi.org/10.1038/s41598-018-19963-1.

Dudek, P. (2013). FDM 3D printing technology in manufacturing composite elements. *Archives of Metallurgy and Materials*, *58*(4), 1415–1418. https://doi.org/10.2478/amm-2013-0186.

El-Sayegh, S., Romdhane, L., & Manjikian, S. (2020). A critical review of 3D printing in construction: Benefits, challenges, and risks. *Archives of Civil and Mechanical Engineering*, *20*(2). https://doi.org/10.1007/s43452-020-00038-w.

Felton, S. M., Tolley, M. T., Shin, B., Onal, C. D., Demaine, E. D., Rus, D., et al. (2013). Self-folding with shape memory composites. *Soft Matter*, *9*(32), 7688–7694. https://doi.org/10.1039/c3sm51003d.

Honarpardaz, M., Tarkian, M., Ölvander, J., & Feng, X. (2017). Finger design automation for industrial robot grippers: A review. *Robotics and Autonomous Systems*, *87*, 104–119. https://doi.org/10.1016/j.robot.2016.10.003.

Jebellat, E., Baniassadi, M., Moshki, A., Wang, K., & Baghani, M. (2020). Numerical investigation of smart auxetic three-dimensional meta-structures based on shape memory polymers via topology optimization. *Journal of Intelligent Material Systems and Structures*, *31*(15), 1838–1852. https://doi.org/10.1177/1045389X20935569.

Khoo, Z. X., Teoh, J. E. M., Liu, Y., Chua, C. K., Yang, S., An, J., et al. (2015). 3D printing of smart materials: A review on recent progresses in 4D printing. *Virtual and Physical Prototyping*, *10*(3), 103–122. https://doi.org/10.1080/17452759.2015.1097054.

Leng, J., Lu, H., Liu, Y., Huang, W. M., & Du, S. (2009). Shape-memory polymers—A class of novel smart materials. *MRS Bulletin*, *34*(11), 848–855. https://doi.org/10.1557/mrs2009.235.

Levy, A., Miriyev, A., Sridharan, N., Han, T., Tuval, E., Babu, S. S., et al. (2018). Ultrasonic additive manufacturing of steel: Method, post-processing treatments and properties. *Journal of Materials Processing Technology*, *256*, 183–189. https://doi.org/10.1016/j.jmatprotec.2018.02.001.

Li, Y., Wang, X., & Yan, G. (2021). Configuration effect and bandgap mechanism of quasi-one-dimensional periodic lattice structure. *International Journal of Mechanical Sciences*, *190*. https://doi.org/10.1016/j.ijmecsci.2020.106017, 106017.

Li, J., Wang, Y., Chen, W., Wang, Y.-S., & Bao, R. (2019). Harnessing inclusions to tune post-buckling deformation and bandgaps of soft porous periodic structures. *Journal of Sound and Vibration*, *459*. https://doi.org/10.1016/j.jsv.2019.114848, 114848.

Mao, Y., Yu, K., Isakov, M. S., Wu, J., Dunn, M. L., & Jerry Qi, H. (2015). Sequential self-folding structures by 3D printed digital shape memory polymers. *Scientific Reports*, *5*. https://doi.org/10.1038/srep13616.

Meaud, J., & Che, K. (2017). Tuning elastic wave propagation in multistable architected materials. *International Journal of Solids and Structures*, *122–123*, 69–80. https://doi.org/10.1016/j.ijsolstr.2017.05.042.

Ngo, T. D., Kashani, A., Imbalzano, G., Nguyen, K. T. Q., & Hui, D. (2018). Additive manufacturing (3D printing): A review of materials, methods, applications and challenges. *Composites Part B: Engineering*, *143*, 172–196. https://doi.org/10.1016/j.compositesb.2018.02.012.

Olakanmi, E. O., Cochrane, R. F., & Dalgarno, K. W. (2015). A review on selective laser sintering/melting (SLS/SLM) of aluminium alloy powders: Processing, microstructure, and properties. *Progress in Materials Science*, *74*, 401–477. https://doi.org/10.1016/j.pmatsci.2015.03.002.

Penumakala, P. K., Santo, J., & Thomas, A. (2020). A critical review on the fused deposition modeling of thermoplastic polymer composites. *Composites Part B: Engineering*, *201*. https://doi.org/10.1016/j.compositesb.2020.108336.

Rayegani, F., & Onwubolu, G. C. (2014). Fused deposition modelling (fdm) process parameter prediction and optimization using group method for data handling (gmdh) and differential evolution (de). *International Journal of Advanced Manufacturing Technology*, *73*(1–4), 509–519. https://doi.org/10.1007/s00170-014-5835-2.

Schmied, J. U., Le Ferrand, H., Ermanni, P., Studart, A. R., & Arrieta, A. F. (2017). Programmable snapping composites with bio-inspired architecture. *Bioinspiration & Biomimetics*, *12*(2). https://doi.org/10.1088/1748-3190/aa5efd.

Shahrubudin, N., Lee, T. C., & Ramlan, R. (2019). An overview on 3D printing technology: Technological, materials, and applications. *Procedia Manufacturing*, *35*, 1286–1296. Elsevier B.V https://doi.org/10.1016/j.promfg.2019.06.089.

Shie, M. Y., Shen, Y. F., Astuti, S. D., Lee, A. K. X., Lin, S. H., Dwijaksara, N. L. B., et al. (2019). Review of polymeric materials in 4D printing biomedical applications. *Polymers*, *11*(11). https://doi.org/10.3390/polym11111864.

Shim, J., Wang, P., & Bertoldi, K. (2015). Harnessing instability-induced pattern transformation to design tunable phononic crystals. *International Journal of Solids and Structures*, *58*, 52–61. https://doi.org/10.1016/j.ijsolstr.2014.12.018.

Shirzad, M., Zolfagharian, A., Matbouei, A., & Bodaghi, M. (2021). Design, evaluation, and optimization of 3D printed truss scaffolds for bone tissue engineering. *Journal of the Mechanical Behavior of Biomedical Materials*, *120*. https://doi.org/10.1016/j.jmbbm.2021.104594, 104594.

Singh, B. K., & Pandey, P. C. (2018). Tunable temperature-dependent THz photonic bandgaps and localization mode engineering in 1D periodic and quasi-periodic structures with graded-index materials and InSb. *Applied Optics*, *57*(28), 8171–8181. https://doi.org/10.1364/AO.57.008171.

Soltani, A., Noroozi, R., Bodaghi, M., Zolfagharian, A., & Hedayati, R. (2020). 3D printing on-water sports boards with bio-inspired core designs. *Polymers*, *12*(1). https://doi.org/10.3390/polym12010249.

Srikantha Phani, A., Woodhouse, J., & Fleck, N. A. (2006). Wave propagation in two-dimensional periodic lattices. *Journal of the Acoustical Society of America*, *119*(4), 1995–2005. https://doi.org/10.1121/1.2179748.

Su, J. W., Tao, X., Deng, H., Zhang, C., Jiang, S., Lin, Y., et al. (2018). 4D printing of a self-morphing polymer driven by a swellable guest medium. *Soft Matter*, *14*(5), 765–772. https://doi.org/10.1039/c7sm01796k.

Sun, W., Ma, Y., Huang, W., Zhang, W., & Qian, X. (2020). Effects of build direction on tensile and fatigue performance of selective laser melting Ti6Al4V titanium alloy. *International Journal of Fatigue*, *130*. https://doi.org/10.1016/j.ijfatigue.2019.105260, 105260.

Sydney Gladman, A., Matsumoto, E. A., Nuzzo, R. G., Mahadevan, L., & Lewis, J. A. (2016). Biomimetic 4D printing. *Nature Materials*, *15*(4), 413–418. https://doi.org/10.1038/nmat4544.

Tibbits, S. (2014). 4D printing: Multi-material shape change. *Architectural Design*, *84*(1), 116–121. https://doi.org/10.1002/ad.1710.

Tobushi, H., Hara, H., Yamada, E., & Hayashi, S. (1996). Thermomechanical properties in a thin film of shape memory polymer of polyurethane series. *Smart Materials and Structures*, *2716*, 483–491. https://doi.org/10.1088/0964-1726/5/4/012.

Wang, Q., Tian, X., Huang, L., Li, D., Malakhov, A. V., & Polilov, A. N. (2018). Programmable morphing composites with embedded continuous fibers by 4D printing. *Materials and Design*, *155*, 404–413. https://doi.org/10.1016/j.matdes.2018.06.027.

Wong, K. V., & Hernandez, A. (2012). A review of additive manufacturing. *International Scholarly Research Notices*, *2012*, 208760.

Yamamura, S., & Iwase, E. (2021). Hybrid hinge structure with elastic hinge on self-folding of 4D printing using a fused deposition modeling 3D printer. *Materials & Design*, *203*. https://doi.org/10.1016/j.matdes.2021.109605, 109605.

Yan, Q., Dong, H., Su, J., Han, J., Song, B., Wei, Q., et al. (2018). A review of 3D printing technology for medical applications. *Engineering*, *4*(5), 729–742. https://doi.org/10.1016/j.eng.2018.07.021.

Zadpoor, A. A., & Malda, J. (2017). Additive manufacturing of biomaterials, tissues, and organs. *Annals of Biomedical Engineering*, *45*(1). https://doi.org/10.1007/s10439-016-1719-y.

Zhang, Z., Demir, K. G., & Gu, G. X. (2019). Developments in 4D-printing: A review on current smart materials, technologies, and applications. *International Journal of Smart and Nano Materials*, *10*(3), 205–224. https://doi.org/10.1080/19475411.2019.1591541.

Zolfagharian, A., Denk, M., Kouzani, A. Z., Bodaghi, M., Nahavandi, S., & Kaynak, A. (2020). Effects of topology optimization in multimaterial 3D bioprinting of soft actuators. *International Journal of Bioprinting*, *6*(2), 1–11. https://doi.org/10.18063/ijb.v6i2.260.

Zolfagharian, A., Kaynak, A., Bodaghi, M., Kouzani, A. Z., Gharaie, S., & Nahavandi, S. (2020). Control-based 4D printing: Adaptive 4D-printed systems. *Applied Sciences*, *10*(9), 3020. https://doi.org/10.3390/app10093020.

Zolfagharian, A., Durran, L., Gharaie, S., Rolfe, B., Kaynak, A., & Bodaghi, M. (2021). 4D printing soft robots guided by machine learning and finite element models. *Sensors and Actuators A: Physical*, *328*. https://doi.org/10.1016/j.sna.2021.112774, 112774.